Structural and magnetic analysis of $Ni_{81}Fe_{19}/Ag$ multilayers with ultrathin $Ni_{81}Fe_{19}$ sublayers

1997 J. Phys.: Condens. Matter 9 4557

(http://iopscience.iop.org/0953-8984/9/22/008)

J. Phys.: Condens. Matter **9** (1997) 4557–4574. Printed in the UK PII: S0953-8984(97)79559-6

Structural and magnetic analysis of $Ni_{81}Fe_{19}$/Ag multilayers with ultrathin $Ni_{81}Fe_{19}$ sublayers

M Chládek†, C Dorner‡, M Matner‡, H Hoffmann‡ and V Valvoda†

† Faculty of Mathematics and Physics, Charles University, Ke Karlovu 5, 12116 Prague 2, Czech Republic

‡ Institut für Experimentelle und Angewandte Physik, Universität Regensburg, Universitätsstrasse 31, 93053 Regensburg, Germany

Received 14 November 1996, in final form 10 February 1997

Abstract. The magnetic and structural properties of $Ni_{81}Fe_{19}$/Ag multilayer films with very thin sublayers of the magnetic $Ni_{81}Fe_{19}$ component, ranging from 5 Å to 10 Å, were studied. A transition from a nearly pure superparamagnetic behaviour ($t_{NiFe} = 5$ Å) to a nearly ferromagnetic behaviour ($t_{NiFe} = 10$ Å) was observed, with a transition at the $Ni_{81}Fe_{19}$ layer thickness of about 7 Å. The observed differences in magnetic properties are thought to be mainly connected with the size of the NiFe particles in the magnetic sublayers, which can be controlled by their thickness. The structure of the magnetic sublayers becomes more disturbed with decreasing thickness, as can be judged from the in-plane correlation length, roughness, and strain, and the numbers of precipitated crystallites of the two components. The influences of various annealing processes were examined, and the structural changes were followed *in situ* by high-angle x-ray diffraction (XRD). The temperature treatment increased the magnetoresistance ratio. We observed a gradual growth of the content of silver and NiFe precipitates with increasing annealing temperature. The structure of the original multilayers gradually deteriorates with increasing temperature, and the whole complex consists of a mixture of residual multilayer blocks and precipitates. The observed structural characteristics of the multilayers under study have been found essential to the understanding of their magnetic properties.

1. Introduction

In recent years, the study of multilayer structures has aroused considerable interest because of the new physical properties of these systems [1]. To understand and optimize the new effects, detailed knowledge of the microstructure and nanostructure of the multilayer films is required. The giant magnetoresistance (GMR) in multilayer films [2–8] and particulate media [9–16] has gained considerable significance in recent years. The magnetoresistance ratio $\Delta R/R$, which describes this effect, depends very sensitively on the structure of the multilayers or the particulate films. The application of the GMR effect as a magnetic sensor is limited by the strength of the applied magnetic field necessary to produce the maximum change of the resistance, as well as by the hysteresis in alternating magnetic fields. Multilayer films of $Ni_{81}Fe_{19}$/Ag or particulate media composed of permalloy precipitates in a silver matrix seem to overcome the problem of large magnetic fields and hysteresis.

A recent paper written by Borchers *et al* [17] indicates that the giant magnetoresistance in 20 Å $Ni_{81}Fe_{19}$/Ag 40 Å multilayers is associated with antiferromagnetic correlations between magnetic domains within NiFe sublayers. These multilayers exhibit very high sensitivity (≈5%) in very low saturation fields ($H_{sat} < 100$ Oe). In this paper, we present

0953-8984/97/224557+18$19.50

the different magnetic effects that occur in $Ni_{81}Fe_{19}$/Ag multilayers with very thin magnetic components, ranging from 5 Å to 10 Å. Statements based on magnetic measurements are confirmed and completed by detailed structure investigations.

XRD provides an especially fast and non-destructive method for studying the structure of multilayers. In the field of low-angle x-ray diffraction (LXRD), various methods have been used to probe the multilayer periods, the density of the materials, the interface roughness, etc. Our efforts were concentrated on the use of new theoretical approaches in XRD, such as evaluating the lateral coherence length of the interface roughness [18]. The distorted-wave Born approximation, a method established for the theoretical treatment of the XRD reflectivity of multilayers [19], is a new approach to the problem of how to take the lateral length scale of the interface roughness into account. Additionally, intra-layer properties (such as the crystallinity, lattice spacings, texture, and strain) can be revealed from the high-angle x-ray diffraction (HXRD) by standard methods, and by fitting with a kinematic model summarized in the computer program SUPREX (superlattice refinement by x-ray diffraction) [20]. Generally, XRD analysis is an 'indirect method', because measured intensities cannot be directly converted into an image of the structure. Therefore, transmission electron microscopy (TEM) and atomic force microscopy (AFM) were used as complementary methods.

2. Experimental details

$Ni_{81}Fe_{19}$/Ag multilayer films with individual $Ni_{81}Fe_{19}$ layer thicknesses from 5 Å to 10 Å, and with a fixed Ag layer thickness of 27 Å, were prepared by rf sputtering onto glass substrates at room temperature. Cr buffer layers with a thickness of 30 Å were deposited to improve the homogeneous growth of the first Ag layer. The deposition rates were 1.0 ± 0.1 Å s^{-1} for $Ni_{81}Fe_{19}$ and 1.2 ± 0.1 Å s^{-1} for Ag and Cr. The background pressure was 5.0×10^{-8} mbar, and the sputtering pressure (99, 98% Ar) was 8.0×10^{-3} mbar. In the following, the film structure is denoted as Cr(30 Å)/[Ag(27 Å)/$Ni_{81}Fe_{19}(t_{NiFe})$]$_{30}$. The films were deposited using the commercial Alcatel deposition instrument. The thickness of the films was controlled by computer-guided shutters, after many calibration tests had been made to ensure the homogeneity and reproducibility of the film thickness.

Magnetization loop measurements, $M(H)$, were performed using a vibrating-sample magnetometer (VSM) and a SQUID magnetometer. The four-point probe method was used for magnetoresistance (MR) measurements up to 5 kOe. External magnetic fields were applied during the VSM and MR measurements either parallel to the film surface (i.e. with the magnetic field parallel to the current: $\boldsymbol{H} \| \boldsymbol{I}$; the in-plane arrangement) or perpendicular to the film surface ($\boldsymbol{H} \perp \boldsymbol{I}$). The VSM and MR measurements were performed at room temperature, and the SQUID hysteresis loops were obtained at different temperatures between 10 K and 300 K.

The measurements in the low-angle XRD region (LXRD) were made by using a RIGAKU 18 kW rotating-anode generator (Cu Kα radiation) and a BEDE double-crystal diffractometer. For the high-angle x-ray diffraction (HXRD) measurements, we used a Philips MRD standard Bragg–Brentano goniometer (Cu Kα radiation) equipped with a secondary graphite monochromator, and Soller slits in the diffracted beam.

The surface topography was measured by a SIS Nanostation atomic force microscope (AFM) in contact mode. TEM cross-sectional images were scanned by a Philips CM30 transmission electron microscope.

The *in situ* x-ray diffraction study was performed using a SIEMENS D500 diffractometer (Co Kα radiation), equipped with a temperature chamber (background pressure: $<1.0 \times$

10^{-7} mbar). The annealing temperature was determined by a thermocouple fixed to a Pt heating element. The real temperature at the relevant spot of the film was calibrated by measuring the lattice parameter of a standard silver powder (using the same substrate). A position-sensitive detector was applied to shorten the acquisition time, and to study the rapid structural changes occurring during the annealing process. The instrumental resolution was calibrated using a standard silver powder.

3. Results of magnetic measurements

In the first part of this section, we present the results of magnetic and magnetoresistive measurements for three different films: Cr(30 Å)/[Ag(27 Å)/$Ni_{81}Fe_{19}(t_{NiFe})$]$_{30}$ with t_{NiFe} = 5 Å, 7 Å, and 10 Å. The silver sublayer thickness was kept at 27 Å, because the magnetoresistance was found to be the highest for this value. A comparison of the as-deposited and annealed samples will be given in the second part of this section.

To obtain more detailed information about the magnetic behaviour of the multilayers with different $Ni_{81}Fe_{19}$ layer thicknesses, we performed temperature-dependent SQUID measurements up to 50 kOe.

The magnetoresistance effect is defined by $\Delta R/R(H) = (R(H) - R_S)/R_S$, where R_S is the resistivity of the magnetically saturated sample. We introduced R_S as the resistance at the maximum available magnetic field of 5 kOe, which is not the saturation field of the samples.

3.1. Magnetic characterization of the as-prepared films

Figure 1 shows magnetization loops and the magnetoresistance at room temperature for three multilayer films with t_{NiFe} = 5 Å, 7 Å, and 10 Å, respectively. The same studies were done on films with t_{NiFe} = 6 Å, 8 Å, and 9 Å, but the results are not shown here, for clarity. The differences between the total signals of the in-plane and perpendicular measurements presented here are due to the different separations between the samples and pick-up coils in the VSM equipment for the in-plane and perpendicular measurements.

The in-plane and perpendicular magnetization loops of the multilayer film with t_{NiFe} = 10 Å (figure 1(a), top) are typical for soft magnetic permalloy films. Quite different behaviour is seen for the magnetization loops of the multilayer film with t_{NiFe} = 5 Å. The magnetization loops for the two directions of the applied field (in-plane and perpendicular—figure 1(a), bottom) show no hysteresis. Saturation is not approached even in fields of 15 kOe.

The sample with t_{NiFe} = 5 Å is probably composed from very small ferromagnetic particles in a non-magnetic Ag matrix. We measured temperature-dependent magnetization loops at different temperatures (T = 300 K, 200 K, 100 K, and 10 K). As shown in figure 2(a), the number of ferromagnetically ordered $Ni_{81}Fe_{19}$ particles, represented by the magnetic moment at H = 0 Oe, increases with decreasing temperature. Due to the relatively broad distribution of different volumes of magnetic particles, more particles become magnetically stable on reducing the temperature. We believe that the sample is superparamagnetic, according to the definition given in [21]. The atomic magnetic moments within each such NiFe particle possess a ferromagnetic order, but the particle as a whole behaves similarly to a paramagnetic atom having a large magnetic moment. Such a behaviour of magnetic particles has been called 'superparamagnetic'.

A fundamental feature of this effect is that the magnetization curves measured at different temperatures should be approximately superposable when plotted with respect to

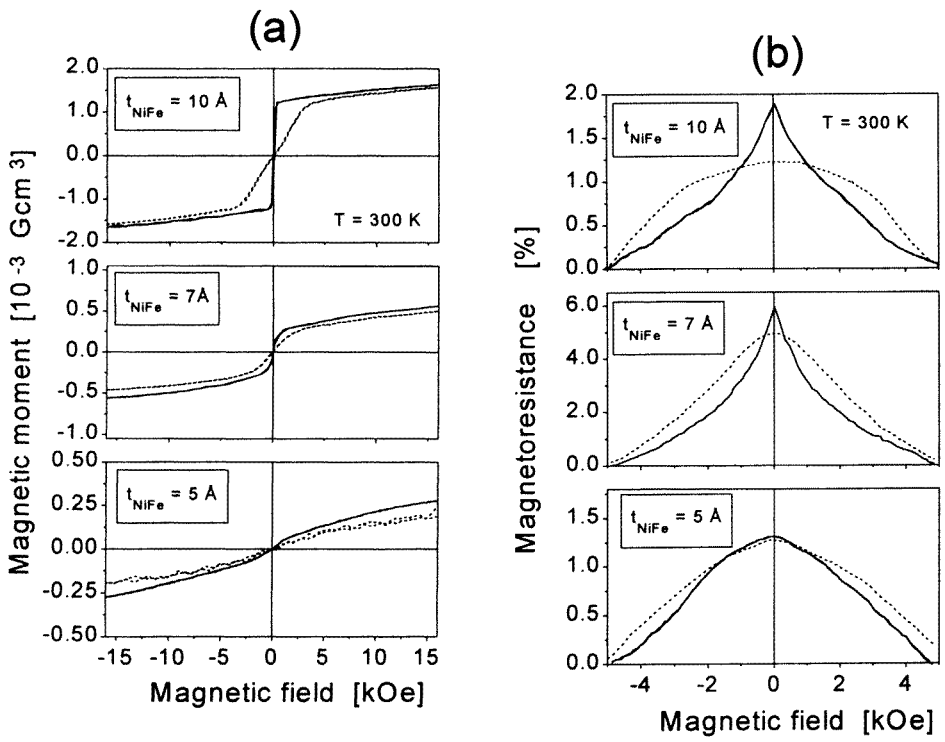

Figure 1. (a) Magnetization loops obtained from VSM measurements of the as-deposited $Ni_{81}Fe_{19}$/Ag multilayer films with $Ni_{81}Fe_{19}$ layer thicknesses of 10 Å, 7 Å, and 5 Å. The magnetic field was applied parallel (——) and perpendicular (– – –) to the plane of the film. (b) Magnetoresistance measurements made with the applied magnetic field parallel (——) and perpendicular (– – –) to the plane of the film for the same samples as in (a). Note the different scales for the magnetic field for (a) and (b).

H/T. Figure 2(b) shows this superposition of the hysteresis loops $M(H)$ taken at different temperatures (T = 100 K, 50 K, and 10 K) and plotted versus H/T. The plausible superposition indicates the superparamagnetic behaviour of this sample.

The magnetization loops of the multilayer with t_{NiFe} = 7 Å (figure 1(a), middle) exhibit the transition between the superparamagnetic system (t_{NiFe} = 5 Å) and the nearly pure ferromagnetic system (t_{NiFe} = 10 Å), where we found an in-plane coercive force $H_C = 0.5$ Oe as determined from magneto-optical Kerr effect (MOKE) measurements.

The magnetoresistance curves are given in figure 1(b). The shapes of the magnetoresistance curves are nearly the same for all of the films in perpendicular fields. The maximum value of $\Delta R/R$ is similar for $t_{\mathrm{NiFe}} = 5$ Å and $t_{\mathrm{NiFe}} = 10$ Å. The system with $t_{\mathrm{NiFe}} = 7$ Å shows much larger values of magnetoresistance, up to $\Delta R/R \approx 6\%$ in a field of 5 kOe, which represents an increase by a factor of 3–5.

For the film with t_{NiFe} = 5 Å, only small differences between the in-plane and perpendicular magnetoresistance are visible (figure 1(b), bottom). The change of the magnetic structure is fairly independent of the direction of the applied field. In contrast, the in-plane and perpendicular curves are quite different in systems with $t_{\mathrm{NiFe}} = 10$ Å layers. The system with $t_{\mathrm{NiFe}} = 7$ Å again shows a transition. The value of $\Delta R/R$ is much larger than that for the films with $t_{\mathrm{NiFe}} = 5$ and 10 Å sublayers.

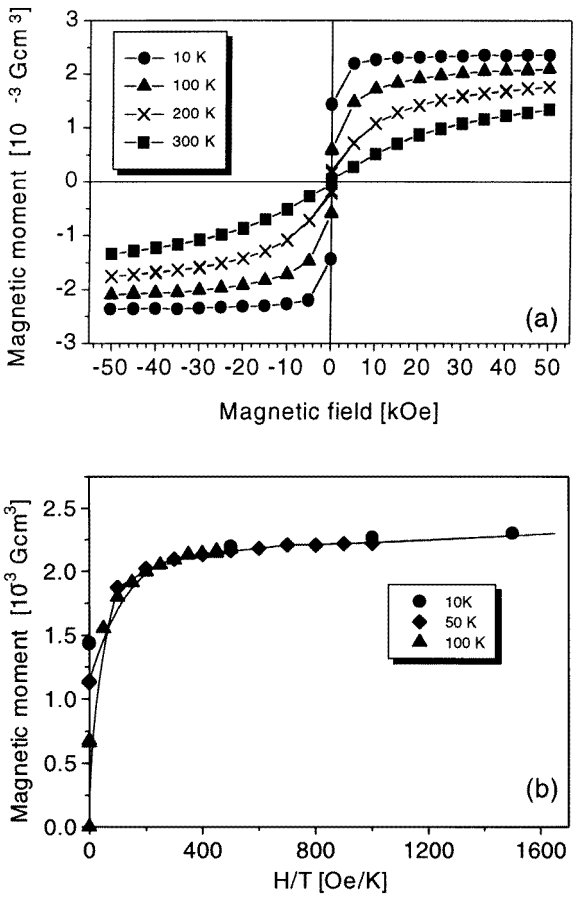

Figure 2. (a) Magnetization loops obtained from SQUID measurements at different temperatures for the sample with a $Ni_{81}Fe_{19}$ layer thickness of 5 Å. (b) The magnetic moment plotted versus the 'normalized' magnetic field, i.e. the ratio of the magnetic field to the temperature for different temperatures for the sample with a $Ni_{81}Fe_{19}$ layer thickness of 5 Å. The solid line is a guide for the eyes.

3.2. Magnetic characterization of the annealed multilayer films

The system Cr(30 Å)/[Ag(27 Å)/$Ni_{81}Fe_{19}$(7 Å)]$_{30}$ revealed a maximum of $\Delta R/R \approx 6\%$. We tried to improve $\Delta R/R$ for this multilayer film by annealing. On varying the temperature conditions, it was established that rapid annealing for 5 min at 435 °C was the most effective treatment. Figure 3 gives the results of the magnetic (figure 3(a)) and the magnetoresistance (figure 3(b)) measurements before and after annealing. The magnetization loops, measured with in-plane and perpendicular magnetic fields, show an increase of the magnetic moment due to annealing. The explanation of this effect follows from the results of the structural investigations (see below). The magnetoresistance increases also upon annealing (figure 3(b)). With the in-plane field, a maximum $\Delta R/R = 7\%$ was measured.

The increase of the magnetoresistance can be attributed, on the one hand, to better conductivity after annealing, resulting in a lower value for the overall resistance R, and therefore in a higher value of $\Delta R/R_{5\ \mathrm{kOe}}$. On the other hand, the better sensitivity of

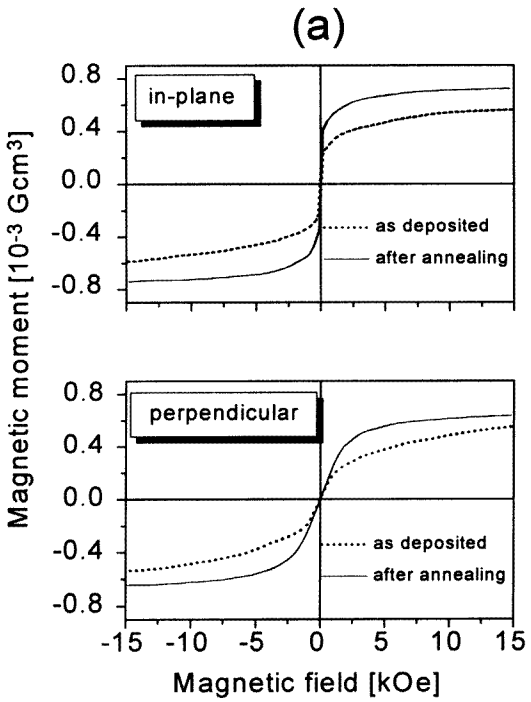

Figure 3. (a) A comparison of the $M(H)$ loops of the as-deposited (– – –) and annealed (——) $Ni_{81}Fe_{19}$/Ag multilayers, each with a $Ni_{81}Fe_{19}$ sublayer thickness of 7 Å. (b) A comparison of the corresponding magnetoresistance curves of the same films as in (a), for the in-plane and perpendicular geometries. The applied magnetic field lies parallel and perpendicular to the plane of the film. Note the different scales for the magnetic field for (a) and (b).

the annealed samples (the narrower magnetoresistance curve) could be attributed to the merging of small superparamagnetic clusters to form larger particles, which results in easier alignment of the magnetization directions by the applied field.

The magnetic measurements give some evidence on the structural properties of thin $Ni_{81}Fe_{19}$/Ag films. To get detailed information about the inter-layer and the intra-layer structure of the samples investigated, we used low-angle and high-angle XRD measurements before, during, and after annealing.

4. Results of the structural analysis of the as-prepared films

4.1. Low-angle x-ray diffraction

Two scanning modes, $\Theta/2\Theta$ scans and Ω scans, were used to measure the specular and diffuse components of the x-ray reflectivity. In $\Theta/2\Theta$ scans, the scattering vector is directed along the sample normal, whereas in Ω scans the scattering vector has components both in the plane and perpendicular to the film surface. Therefore, Ω scans can be used to probe the diffuse reflectivity, which provides information about the lateral correlation lengths of the interface roughness profiles. In the $\Theta/2\Theta$ geometry, the specular reflectivity and the fraction of the diffuse reflectivity scattered in the specular direction are measured. The

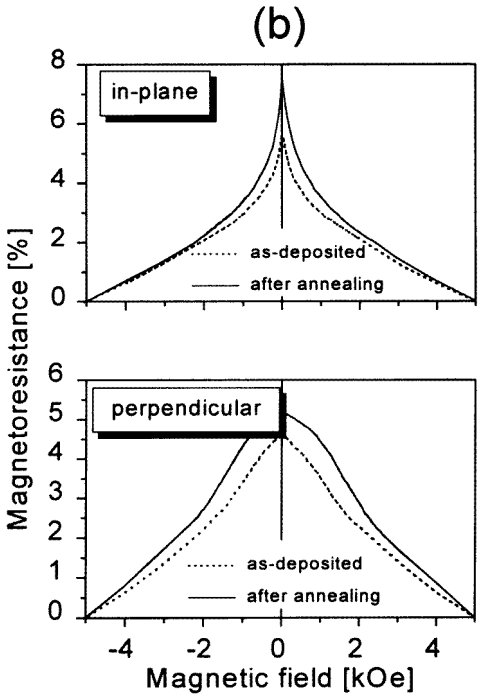

Figure 3. (Continued)

specular reflectivity yields information about the r.m.s. roughness of the interfaces, and the model calculations used are based on the approach of Névot and Croce [22]. The distorted-wave Born approximation (DWBA) [23], introduced by Holý *et al* [19] for multilayers, is a very suitable formalism for describing the non-specular scattering at rough multilayers.

Reflectivity profiles for the as-grown films with 5 Å, 7 Å, and 10 Å permalloy layer thickness were fitted using the above-mentioned models. Figure 4 shows measured and simulated low-angle $\Theta/2\Theta$ and Ω scans. The small multilayer period Λ shifts the multilayer peaks to higher angles. The separation of Kiessig's fringes is very small, due to the high total thickness of the films. Both of these factors result in the reflectivity profiles having only one or two multilayer peaks, and small fringes.

We used a cumulative-roughness model [19], where the roughness of each interface j (counted from the air) is generally given by an interfacial roughness, σ_N, replicated from sublayer to sublayer, plus an intrinsic roughness, $\Delta\sigma$, introduced during the growth of the multilayer:

$$\sigma_j = \sqrt{\sigma_N^2 + (N - j)\Delta\sigma^2}. \tag{1}$$

N denotes the number of interfaces in the periodic multilayer, and σ_N is the roughness of the substrate (interface N). For simplicity, we assume the same in-plane correlation length ξ for all roughness profiles in a given multilayer. The parameter h, included in the DWBA and describing the fractal dimension $D = 3 - h$ of the interfaces, was fixed to the value 1. This implies that the roughness profile is Gaussian-like, which means that it is relatively smooth, and not jagged [24].

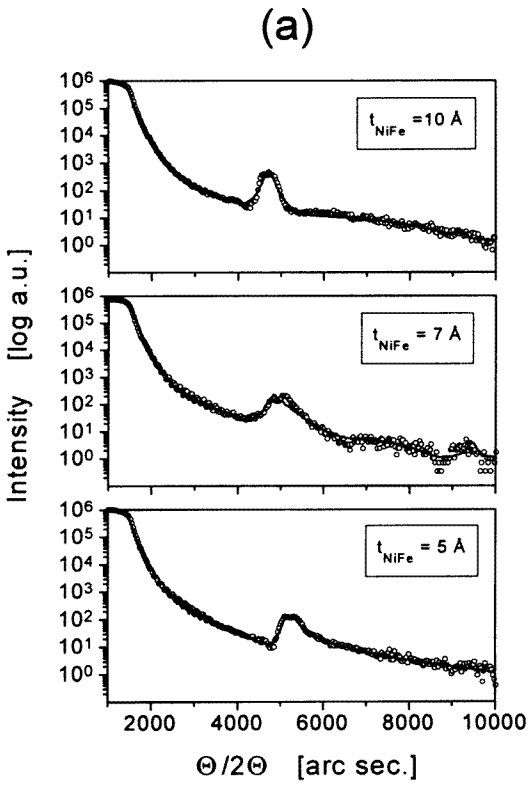

Figure 4. Measured (○) and fitted LXRD profiles (——) for as-deposited $Ni_{81}Fe_{19}$/Ag multilayer films with t_{NiFe} = 10 Å, 7 Å, and 5 Å. Θ/2Θ scans are shown in (a), and the corresponding Ω scans, taken at the multilayer peak position, are presented in (b).

Table 1. The roughness and inter-layer structure properties for the multilayer films with t_{NiFe} = 10 Å, 7 Å, and 5 Å. The parameters were evaluated by means of a joint DWBA refinement of the Θ/2Θ and Ω scans, shown in figure 4.

Parameter	$t_{NiFe} = 10$ Å	$t_{NiFe} = 7$ Å	$t_{NiFe} = 5$ Å
Multilayer period, Λ (Å)	35.0 ± 0.2	34.1 ± 0.3	31.9 ± 0.2
Ratio t_{NiFe}/t_{Ag}	0.32 ± 0.1	0.25[a]	0.19[a]
NiFe oxide thickness (Å)	10[a]	7[a]	5[a]
Density, $\rho_{NiFe\,oxide}$ (%)[b]	63 ± 1	62 ± 2	62[a]
Top roughness, σ_{top} (Å)	24 ± 1	22 ± 3	33 ± 10
Mean roughness, σ (Å)	14 ± 5	16 ± 6	13 ± 4
In-plane correlation length, ξ (Å)	460 ± 30	360 ± 50	200 ± 30

[a]A parameter fixed during the fit.
[b]This refers to the bulk values.

The main refined parameters obtained from fitting the Θ/2Θ and Ω scans are shown in table 1. The relative densities of the materials Ag and $Ni_{81}Fe_{19}$, affecting the refractive indices, are in the range 94% to 102% of the bulk values for each of the samples investigated. Modified $Ni_{81}Fe_{19}$ layers with a reduced density on the top of each multilayer were taken into account, due to the expected oxidation of the sample surfaces. The multilayer periods

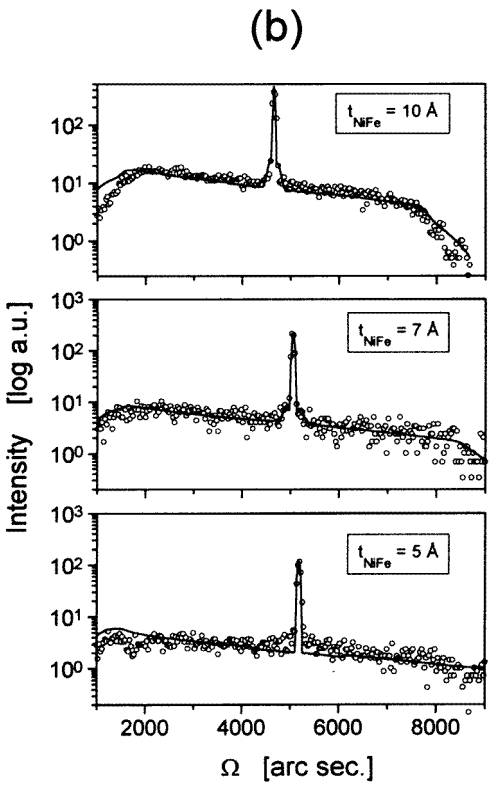

Figure 4. (Continued)

determined, Λ, are in good agreement with the values obtained by HXRD (see table 2).

The mean roughnesses over all of the interfaces for each sample studied were determined to take values of about 15 Å. The interface roughness near the substrate is a few Å, and the roughness accumulation leads to values of more than 20 Å for interfaces near the surfaces of the samples.

From the refinement of the Ω scans, we established that the in-plane correlation length scales with the $Ni_{81}Fe_{19}$ layer thickness. In the film with a 5 Å $Ni_{81}Fe_{19}$ layer thickness, the in-plane correlation length is about 200 Å, in the film with a 7 Å layer thickness it is about 360 Å, and it is roughly 460 Å for the sample with 10 Å of $Ni_{81}Fe_{19}$. We checked the results obtained for the sample with 7 Å of $Ni_{81}Fe_{19}$ by obtaining TEM cross-sectional images and AFM scans, and a good agreement was found (see section 4.3, figure 6, and figure 7).

4.2. High-angle x-ray diffraction

In general, superlattice peaks can be observed in HXRD $\Theta/2\Theta$ scans, if the structural coherence length Γ normal to the layer plane is larger than the multilayer period Λ. The positions of the peaks are determined by equation (2), where n is an integer which labels the order of the satellite around the main Bragg peak, and $\bar{d} = \Lambda/(N_{Ag} + N_{NiFe})$, where N_{Ag} and N_{NiFe} are the numbers of atomic planes of the materials Ag and $Ni_{81}Fe_{19}$ in one

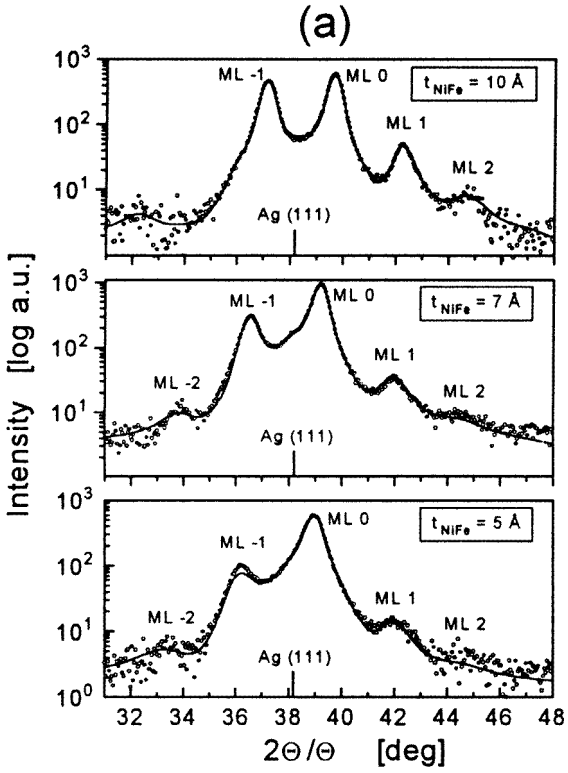

Figure 5. (a) Measured satellites around the (111) fcc reflection (○), and the result of the SUPREX refinement (——) for the as-deposited samples with 10 Å, 7 Å, and 5 Å $Ni_{81}Fe_{19}$ layer thickness. The peaks are indexed according to equation (2). Please note the logarithmic scale. (b) Satellites measured around the (222) fcc reflection (○) and the calculated curves (——). The peaks are indexed according to equation (2) with $\bar{d}_{222} = \bar{d}_{111}/2$. All of the parameters are summarized in table 2.

bilayer:

$$\frac{2\sin\Theta}{\lambda_{\mathrm{x-ray}}} = \frac{1}{\bar{d}} \pm \frac{n}{\Lambda}. \tag{2}$$

In the following, all multilayer peaks are indexed according to this equation as MLn (i.e. ML-2, ML-1, etc).

Satellites around the (111) fcc reflection, and an intensity modulation around the (222) fcc peak are visible in all of the measured patterns (see figure 5). This indicates that the grains of the polycrystalline samples are strongly textured. The full widths at half-maximum (FWHM) of the Ω scans at the (111) reflection position were in the range from 8.0° to 8.6° for all of the samples. This implies that the (111) planes of crystallites are not perfectly parallel to the film surface. Pole figures showed a random grain orientation around the texture axis (fibre texture).

We performed a quantitative analysis of the $\Theta/2\Theta$ scans by using the refinement program SUPREX to get detailed information about the microstructure of the $Ni_{81}Fe_{19}$/Ag multilayers investigated.

Both diffraction orders, shown in figure 5, were measured, to render possible a simult-

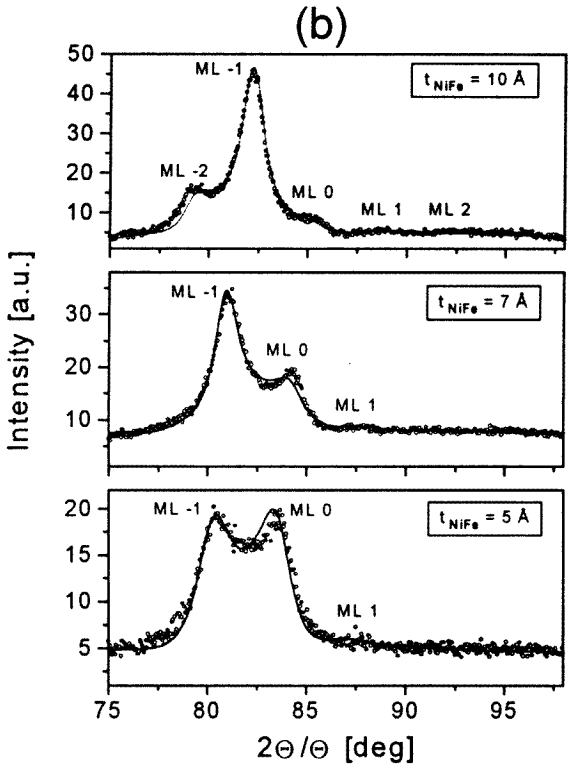

Figure 5. (Continued)

Table 2. Summarized parameters from the SUPREX refinement for the NiFe/Ag multilayers with $t_{NiFe} = 10$ Å, 7 Å, and 5 Å.

Parameter	$t_{NiFe} = 10$ Å	$t_{NiFe} = 7$ Å	$t_{NiFe} = 5$ Å
Multilayer period, Λ (Å)	36.3	33.7	31.1
Ratio t_{NiFe}/t_{Ag}	0.46	0.33	0.29
Interface width, a (Å)	2.32	2.29	2.24[a]
Continuous disorder, c (Å)	0.1	0.12	0.1[a]
No of Ag lattice planes, $N_{Ag} \pm \Delta N_{Ag}$	10.6 ± 1.6	10.7 ± 2.1[a]	10.4 ± 1.9
ΔN_{Ag}, second order	1.9	2.2[a]	2.8
No of NiFe lattice planes, $N_{NiFe} \pm \Delta N_{NiFe}$	5.5 ± 0.2	4.0 ± 0.6	3.0 ± 1.2[a]
ΔN_{NiFe}, second order	0.1[a]	0.7	1.1
Ag fcc (111) lattice spacing, d_{Ag} (Å)	2.356	2.366	2.365
NiFe fcc (111) lattice spacing, d_{NiFe} (Å)	2.066	2.072	2.122
Average lattice spacing, $\bar{d}$ (Å)	2.27	2.30	2.31

[a]A parameter fixed during the fit.

aneous refinement with the same fitting parameters for the first and second order, except the discrete disorder. We used the smallest possible number of free fitting parameters, because the presence of an additional Ag (111) peak introduced four more parameters. Therefore, we avoided using asymmetrical strain profiles. The fitted parameters are summarized in table 2, and the results of the refinement are plotted in figure 5 (the solid line).

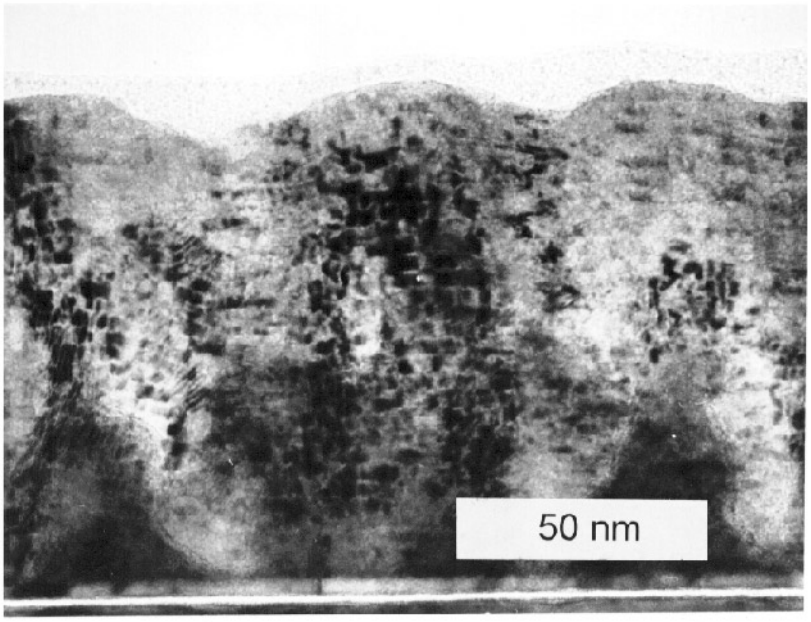

Figure 6. A cross-sectional TEM micrograph of a Cr(30 Å)/[Ag(27 Å)/$Ni_{81}Fe_{19}$(7 Å)]$_{30}$ as-deposited multilayer film on a silicon substrate; beam voltage: 300 kV.

The intensity of the Ag peak grows with decreasing thickness of the $Ni_{81}Fe_{19}$ layers. The width of this peak is much smaller than the width corresponding to the 27 Å vertical dimension of the Ag sublayers. The ratios of the Ag peak intensity to the strongest satellite peak were 0.05 for $t_{NiFe} = 10$ Å, 0.11 for $t_{NiFe} = 7$ Å, and 0.12 for $t_{NiFe} = 5$ Å. This indicates that the $Ni_{81}Fe_{19}$ layers are not completely homogeneous over the whole multilayer stack in the lateral direction, because of the presence of Ag crystallites with vertical sizes of hundreds of Å. The $Ni_{81}Fe_{19}$ (111) reflection is probably overlapped and too weak for detection, due to the lower scattering power and lower proportion of diffracting material. The average coherence length of the multilayer structure perpendicular to the film surface is $\Gamma \approx 250$ Å for all of the samples. We determined this value from standard powder analysis, where we separated Gaussian and Lorentzian contributions to the linewidths (the single-peak method [25]). We assumed that the Lorentzian contribution was caused by the grain size effect. The value obtained is in good agreement with TEM images (see figure 6), and with our previous work [26], as well. This confirms that the multilayer stack is not completely homogeneous over the total thickness of about 1000 Å in each multilayer.

The thicknesses of the Ag layers refined by SUPREX are nearly the same for all of the samples, and are about 2 Å lower than designed. The $Ni_{81}Fe_{19}$ layers seem to be slightly thicker than was intended. In the case of the sample with 5 Å $Ni_{81}Fe_{19}$ layer thickness, the number of $Ni_{81}Fe_{19}$ atomic layers was a very unstable parameter. We fixed the value at three monolayers, which corresponds to the as-designed value. The fit for the first order is not optimal (at the ML-1 peak), but we took into account the fact that the ratio N_{NiFe}/N_{Ag} is very sensitive for the peak intensity of the second order, where very good agreement was reached. Nevertheless, the film with 5 Å $Ni_{81}Fe_{19}$ layer thickness proves to be a very much distorted multilayer.

The discrete disorder parameters (ΔN_{Ag} and ΔN_{NiFe}) are suitable for using to compare the interface disorders. We used the approach presented by Fullerton *et al* [20]. Different discrete disorders for the first- and second-order satellites were allowed, because the second-order peaks are more sensitive. Nevertheless, the difference found is small. As expected, the discrete disorder grows with decreasing thickness of the $Ni_{81}Fe_{19}$ layers, which implies that the $Ni_{81}Fe_{19}$ layers are strongly distorted in the sample with 5 Å $Ni_{81}Fe_{19}$ sublayer thickness.

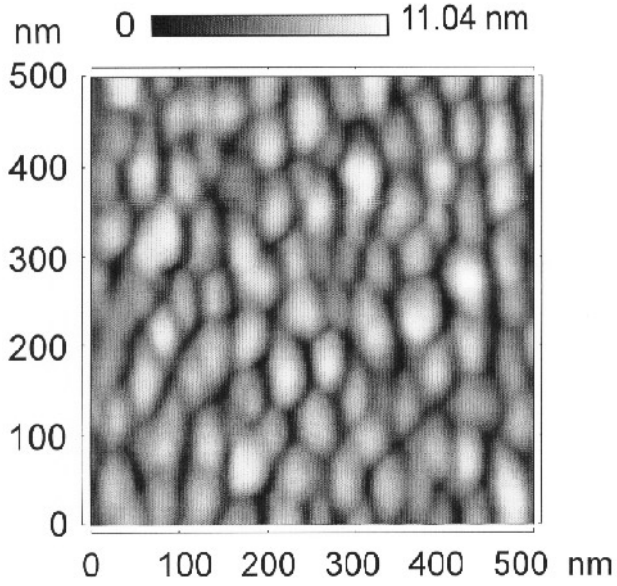

Figure 7. A grey-scale image of the AFM topography of the $Ni_{81}Fe_{19}/Ag$ multilayer surface with 7 Å $Ni_{81}Fe_{19}$ sublayer thickness. The scale is 110 Å from dark to white, and the scan area is 5000×5000 Å^2.

The discrete disorder, obtained by HXRD analysis, is comparable with the LXRD interface roughness if the in-plane correlation length has similar values. In our case, XRD reflectivity in the low-angle regime 'sees' the long-range roughness (figure 6 and figure 7) that is comparable with the in-plane grain size. In contrast, the discrete disorder indicates the fluctuation of the layer thickness inside these grains.

The lattice spacing of Ag (bulk value: 2.359 Å) refined by SUPREX remains nearly stable for all of the samples measured, whereas the lattice spacing of $Ni_{81}Fe_{19}$ (bulk value: 2.048 Å) grows with decreasing thickness. This corresponds to the increased compressive strain in the $Ni_{81}Fe_{19}$ layers.

4.3. AFM and TEM

The TEM cross-sectional image in figure 6 shows rather smooth interfaces near the substrate, but the upper layers appear to be very rough. This confirms very well the cumulative-roughness model used in the LXRD analysis. The roughness is caused by grains with an average diameter of about 500 Å, forming smooth hills and valleys. Their size approximately corresponds to the in-plane correlation length $\xi \cong 360$ Å, obtained from LXRD analysis.

We used the AFM surface topography of the same film to quantify the in-plane

correlation length, and the roughness of the sample surface. The vertical and horizontal analysis of a typical topography, shown in figure 7, yields a surface roughness of 22.5 Å $\pm$ 2.0 Å, and a average grain size of 410 Å $\pm$ 80 Å. These values are in very good agreement with the results obtained from LXRD and TEM, respectively.

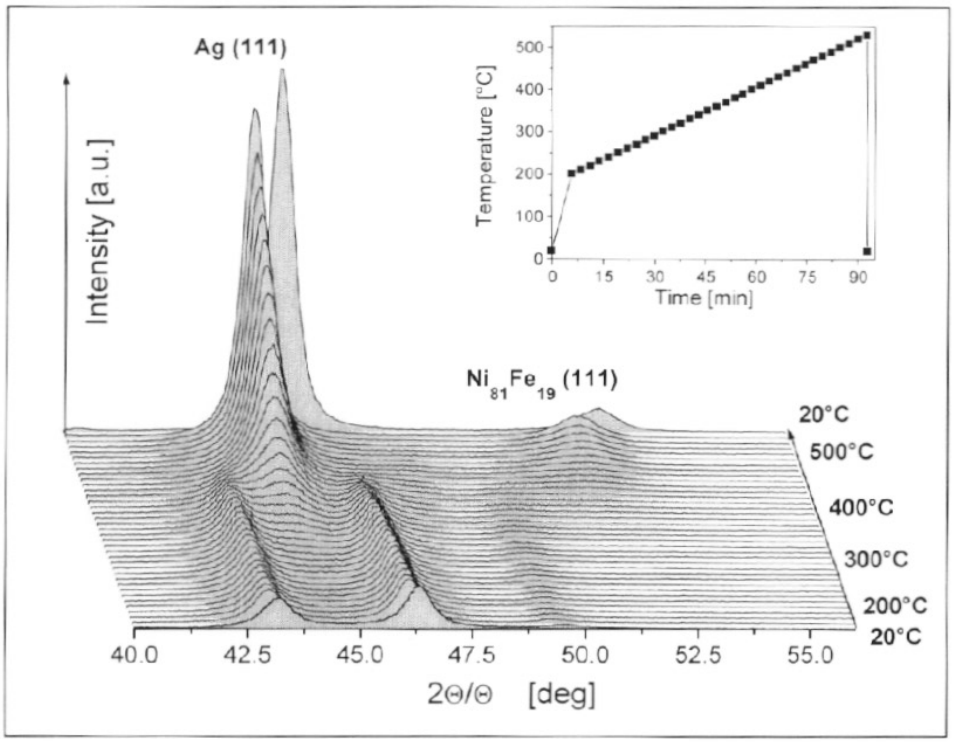

Figure 8. *In situ* HXRD patterns for the sample with a $Ni_{81}Fe_{19}$ layer thickness of 10 Å, during the annealing process, which is shown in the inset. The pattern at the back was taken at room temperature after the annealing process.

5. Results for *in situ* HXRD during annealing

For the samples analysed in section 4, we investigated the structure changes induced during a long annealing process to obtain information about the growth morphology. First, we increased the temperature to 200 °C over an interval of about 300 s. Subsequently, the samples were annealed in the range 200–530 °C at an annealing rate of about 0.07 °C s^{-1}. Figure 8 summarizes the $2\Theta/\Theta$ scans measured successively with increasing temperature for the sample with 10 Å $Ni_{81}Fe_{19}$ layer thickness. The inset shows the variation of the temperature during the annealing process. As was already shown earlier, a small Ag peak is present in all of the patterns, but at a temperature of about 350 °C, Ag(111) and $Ni_{81}Fe_{19}$ (111) peaks start growing significantly. Finally, the Ag and $Ni_{81}Fe_{19}$ peaks dominate the profiles, and only very weak residua of the multilayer peaks can be seen at the base of the Ag(111) reflection. Patterns taken for the samples with 7 Å $Ni_{81}Fe_{19}$ and 5 Å $Ni_{81}Fe_{19}$ layer thicknesses show very similar behaviour, except that the strong increase of the Ag peaks

starts earlier, at 340 °C and 320 °C, respectively. These results agree well with resistivity measurements made during annealing (not shown here), where a steep drop of resistivity is observed, i.e. at a temperature of about 350 °C for the films with 7 Å $Ni_{81}Fe_{19}$ layer thickness. This can be attributed to the significant growth of the Ag crystallites.

Selected measured patterns were fitted with Pearson-VII functions [27]. Figure 9 presents the fitted heights (a) and the full widths at half-maximum (b) for the measured multilayer peaks. In our recent work [26], we observed that the heights of the satellite peaks grow slowly until the temperature of 320 °C is reached, due to the healing of the multilayer structure. In this study, we can find this effect occurring weakly in the sample with 10 Å $Ni_{81}Fe_{19}$ sublayer thickness, but not in the other samples. Above the temperature of 300 °C, deterioration of the multilayer structure for these samples continues, and the FWHM of these peaks grow correspondingly.

This fact leads to the conclusion that, for the samples in which $Ni_{81}Fe_{19}$ is nearly homogeneous over the multilayer stack, the annealing process heals the multilayer structure until a temperature of about 340 °C is reached (the sample with $t_{NiFe} = 10$ Å). The distorted multilayers (the samples with $t_{NiFe} = 5$, 7 Å) are not affected too much by lower temperatures. We suppose that the layer structure deteriorates when the atomic mobility is sufficient in high-diffusivity paths, especially at grain boundaries and in other distorted areas.

We used the fitted multilayer peak positions to calculate the average lattice spacing $\bar{d}$ and the multilayer period Λ as functions of the temperature (equation (2)). The experimental values were compared with a simulated temperature dependence of $\Lambda = N_{NiFe}d_{NiFe} + N_{Ag}d_{Ag}$ and $\bar{d} = \Lambda/(N_{NiFe} + N_{Ag})$. These were calculated with the lattice spacings d_{Ag}, d_{NiFe}, which are determined by the lattice expansion coefficients given by [28]. The parameters N_{NiFe} and N_{Ag} were refined with the computer program SUPREX from the patterns measured at room temperature. Comparing these curves, we found that the multilayer structure has expanded according to the lattice expansion of the individual materials in the temperature range from 20 °C to about 300 °C. Then we observed a significant reduction of the average lattice spacing, $\bar{d}$. This decrease demonstrates the relaxation of the lattice misfit at the interfaces. We found that the parameters Λ and $\bar{d}$ are very sensitive as regards detection of the changes in the multilayers induced by the annealing process.

From the Ag(111) peak positions and peak widths, we found that all of the growing Ag crystallites are in compressive stress during annealing, which may result from the growth of Ag bridges at the multilayer grain boundaries. Increasing temperature diminishes this effect, and after annealing there is a slightly tensile stress at room temperature, due to different thermal contractions of the film and the substrate during cooling. A similar analysis for the optimized temperature process was carried out as well. Results will be published elsewhere.

6. Discussion and conclusions

$Ni_{81}Fe_{19}/Ag$ multilayer films with individual $Ni_{81}Fe_{19}$ layer thicknesses from 5 Å to 10 Å, and with a fixed Ag layer thickness of 27 Å, show the giant magnetoresistance effect (GMR). The maximum value of the GMR was found to be 6% at 5 kOe for $t_{NiFe} = 7$ Å and $t_{Ag} = 27$ Å, where the transition from the paramagnetic-like behaviour at $t_{NiFe} = 5$ Å to the nearly pure ferromagnetic state at $t_{NiFe} = 10$ Å occurs in characteristic magnetization loops. The multilayers with $t_{NiFe} = 10$ Å show the in-plane and perpendicular magnetization loops known to occur for continuous soft magnetic films with shape anisotropy.

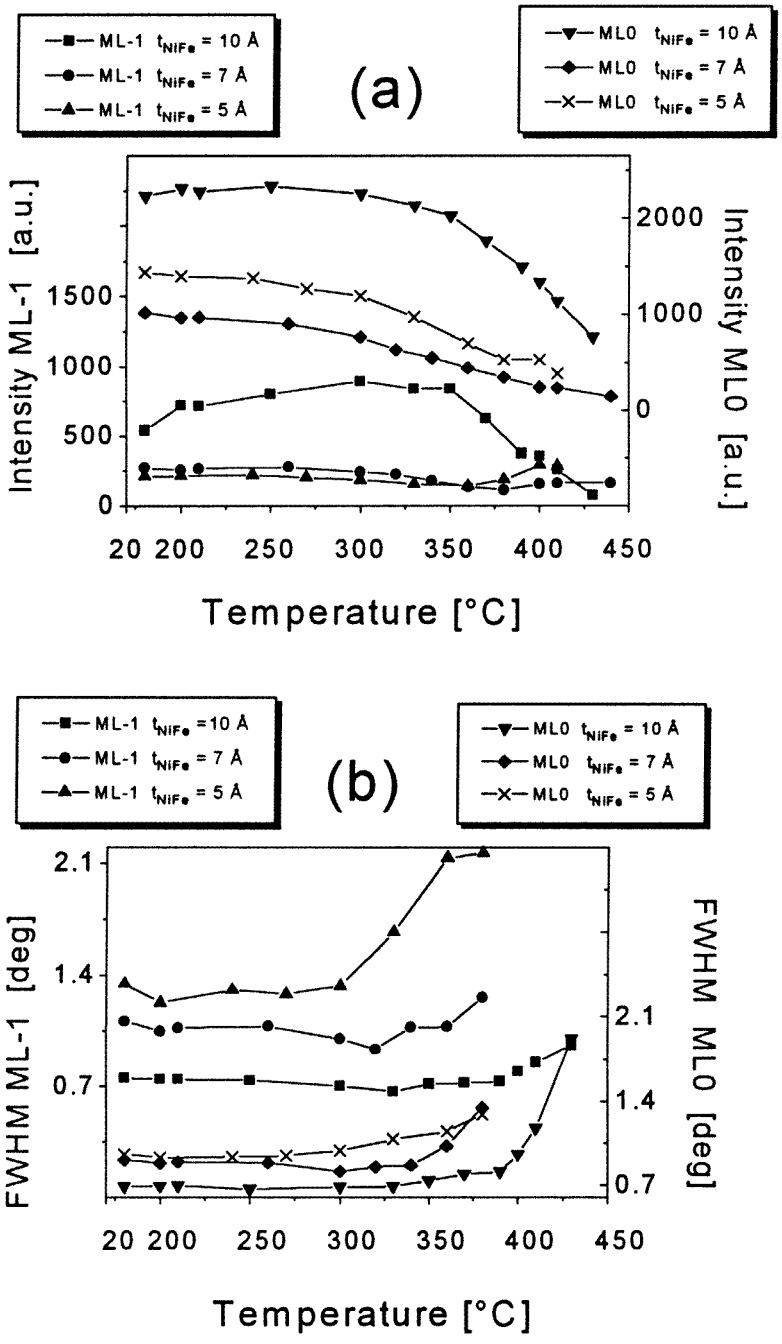

Figure 9. (a) Fitted multilayer peak heights, ML−1, ML0, for the multilayers with 10 Å, 7 Å, and 5 Å $Ni_{81}Fe_{19}$, as functions of the annealing temperature. The curve ML−1 for the sample with 10 Å $Ni_{81}Fe_{19}$ was shifted by −1000 for clarity. Please note the different scale on the right. (b) The FWHM for the same peaks (left for ML−1 peaks, right for ML0 peaks). Note the different scale on the right.

Quite different magnetic behaviour for the sample with $t_{NiFe} = 5$ Å was found using temperature-dependent magnetization loops. This multilayer is composed from very thin NiFe sublayers in the non-magnetic Ag matrix, and we believe that these sublayers are probably small ferromagnetic particles disordered by thermal fluctuations, and therefore called superparamagnetic according to [21]. A simple reciprocal relation between the absolute temperature T and the volume of the particle V gives under simplified assumptions a condition [29] for this state: $kT/V > c$, where k is the Boltzmann constant and c is a number. The temperature-dependent magnetization loops confirm the transition, when at 10 K all of the magnetic particles are saturated. The temperature range for the transition is broad. This suggests that the distribution of volumes of particles in the sample is broad too. Additional evidence was given in figure 2(b), where we have shown that the magnetization curves were superposable when plotted with respect to H/T. At room temperature, the condition for the superparamagnetic state is broken at the thickness of $t_{NiFe} = 7$ Å, due to the larger volume of NiFe particles in comparison with the 5 Å case. It is evident that the transition is not sharp, because there is probably a broad distribution of particulate volumes.

The structure analysis proves the above-mentioned conclusions well. As detected by LXRD, strong cumulative roughness is present in all of the multilayers, and the lateral correlation length decreases from 460 Å to 200 Å with decreasing thickness of the permalloy layers. The values give a measure for the lateral grain size, as confirmed by TEM and AFM, as well. Looking inside these grains by using HXRD, the volume fraction of the $Ni_{81}Fe_{19}$ precipitates and 'bridging' Ag crystallites is seen to increase in films with thinner NiFe sublayers. In the remaining multilayer blocks, the layer materials exhibit stress that is more compressive, and fluctuations in the number of atomic planes.

The above-mentioned facts mean that the multilayer structure of the sample with $t_{NiFe} = 10$ Å is well developed. The NiFe sublayers are not distorted inside the grains too much, and they can form long lateral ferromagnetic sublayers. On the other hand, the sample with $t_{NiFe} = 5$ Å has a very disrupted multilayer structure, indicating that the $Ni_{81}Fe_{19}$ layers are flat magnetic particles in an Ag matrix. Nevertheless, we found that a periodic structure is partially present in the film. The transition structure in the sample with $t_{NiFe} = 7$ Å with flat particles forming discontinuous ferromagnetic layers seems to be favourable as regards achieving higher magnetoresistance.

By annealing in different temperature conditions, we were able to increase the ratio $\Delta R/R$ up to 7%. The samples with 5 Å and 7 Å $Ni_{81}Fe_{19}$ layer thicknesses do not demonstrate any healing effect [26], and the multilayer structure is so much distorted that deterioration starts as soon as the atom mobility is high enough. Growing Ag crystallites are under compressive stress. This indirectly supports their main location at grain boundaries between the grains of multilayer blocks. The effect of creation of silver bridges was observed by Parker *et al* [14] in TEM micrographs. Their growth indicates the degree of distortion of an annealed multilayer. The measured and simulated behaviour of the average lattice spacing $\bar{d}$ and the multilayer period Λ characterizes the thermal behaviour of an annealed multilayer. We found that the expected thermal expansion holds well in the temperature range from 20 °C to about 300 °C. The above-described *in situ* structure analysis at elevated temperatures enabled us to optimize the annealing conditions.

Acknowledgments

We would like to thank V Holý for providing us with the basic version of the refinement program DWBA, K Závěta for very helpful discussions, R Fischer for the preparation of the TEM cross-sectional images, and T Borst for performing the AFM measurements. We

especially thank A Buchal for providing us with the possibility of performing the *in situ* XRD measurements. We would also like to thank M Gumberger for the preparation of the samples. The refinement program SUPREX was developed with funds provided by the US Department of Energy, and the Belgian Inter-university Attraction Pole Program. Two of us (M Chládek and V Valvoda) also acknowledge grant support from Charles University, and from the US–Czechoslovak Science and Technology Joint Fund (grant No 93008).

References

[1] See, e.g.,
Dhez P and Weisbuch C (ed) 1988 *Physics, Fabrication and Application of Multilayered Structures* (Amsterdam: North-Holland)
or
Chamberod A and Hillairet J (ed) 1990 *Metallic Multilayers (Materials Science Forum 59–60)* (Zürich: Trans Tech Publications)
[2] Baibich M N, Broto J M, Fert A, Nguyen van Dau F, Petroff F, Etienne P, Creuzet G, Friederich A and Chazelas J 1988 *Phys. Rev. Lett.* **61** 2472
[3] Binasch G, Grünberg P, Saurenbach F and Zinn W 1989 *Phys. Rev.* B **39** 4828
[4] Grünberg P, Demokritov S, Fuss A, Vohl M and Wolf J A 1991 *J. Appl. Phys.* **69** 4789
[5] Parkin S S P, Bhadra R and Roche K P 1991 *Phys. Rev. Lett.* **66** 2152
[6] Parkin S S P, More N and Roche K P 1990 *Phys. Rev. Lett.* **64** 2304
[7] Parkin S S P 1992 *Appl. Phys. Lett.* **60** 512
[8] Dorner C, Haidl H and Hoffmann H 1993 *J. Appl. Phys.* **74** 5886
[9] Rodmacq B, Palumbo G and Gerard P 1993 *J. Magn. Magn. Mater.* **118** L11
[10] Bian X, Altounian Z, Ström-Olson J O, Zaluska A, Huai Y and Cochrane R W 1994 *J. Appl. Phys.* **75** 6560
[11] Bian X, Meng X, Ström-Olsen J O, Altounian Z, Muir W B, Sutton M and Cochrane R W 1994 *J. Appl. Phys.* **76** 6796
[12] Coffey K R, Hylton T L, Parker M A and Howard J K 1993 *Appl. Phys. Lett.* **63** 1579
[13] Hylton T L, Coffey K R, Parker M A and Howard J K 1994 *J. Appl. Phys.* **75** 7058
[14] Parker M A, Hylton T L, Coffey K R and Howard J K 1994 *J. Appl. Phys.* **75** 6382
[15] Parker M A, Coffey K R, Howard J K, Tsang C H, Fontana R E and Hylton T L 1996 *IEEE Trans. Magn.* **32** 142
[16] Stearns M B and Cheng Y 1994 *J. Appl. Phys.* **75** 6894
[17] Borchers J A, Gehring P M, Erwin R W, Majkrzak C F, Anke J F, Hylton T L, Coffey K R, Parker M A and Howard J K 1996 *J. Appl. Phys.* **79** 4762
[18] Temst K, Bael M J, Wuyts B, Van Haesendonck C, Bruynseraede Y, de Groot D G, Koeman N and Griessen R 1995 *Appl. Phys. Lett.* **67** 3429
[19] Holý V, Kuběna J, Ohlídal I, Lischka K and Plotz W 1993 *Phys. Rev.* B **47** 15 896
[20] Fullerton E E, Schuller I K, Vanderstraeten H and Bruynseraede Y 1992 *Phys. Rev.* B **45** 9292
[21] Bean C P and Jacobs I S 1956 *J. Appl. Phys.* **27** 1448
[22] Névot L and Croce P 1980 *Revue Phys. Appl.* **15** 761
[23] Sinha S K, Sirota E B, Garoff S and Stanley H B 1988 *Phys. Rev.* B **38** 2297
[24] See, e.g.,
de Boer D K G 1993 *Phys. Rev.* B **49** 5817
[25] de Keijser T H and Langford J I 1982 *J. Appl. Crystallogr.* **15** 308
[26] Chládek M, Dorner C, Buchal A, Valvoda V and Hoffmann H 1996 *J. Appl. Phys.* **80** 1437
[27] Kužel R 1992 *Computer Program DIFPATAN* Faculty of Mathematics and Physics, Charles University, Prague, Czech Republic
[28] Pearson W B 1958 *A Handbook of Lattice Spacings and Structures of Metals and Alloys* Part I (London: Pergamon)
Pearson W B 1967 *A Handbook of Lattice Spacings and Structures of Metals and Alloys* Part II (London: Pergamon)
[29] Néel L 1953 *Rev. Mod. Phys.* **25** 293